Journal of the Taiwan Institute of Chemical Engineers 162 (2024) 105560

Contents lists available at ScienceDirect

Journal of the Taiwan Institute of Chemical Engineers

journal homepage: www.journals.elsevier.com/journal-of-the-taiwan-institute-of-chemical-engineers

Crystal structure and thermoelectric properties of mechanically activated $LaCoO_3$

Vyacheslav A. Dudnikov [a], Yuri S. Orlov [a,b,*], Leonid A. Solovyov [c], Sergey N. Vereshchagin [c], Yuri N. Ustyuzhanin [a], Sergey M. Zharkov [a,b], Galina M. Zeer [b], Andrey A. Borus [a], Vitaly S. Bondarev [a,b], Sergey G. Ovchinnikov [a,b]

[a] Kirensky Institute of Physics, Federal Research Center KSC SB RAS, Krasnoyarsk, 660036, Russia
[b] Siberian Federal University, Krasnoyarsk, 660041, Russia
[c] Institute of Chemistry and Chemical Technology, Federal Research Center KSC SB RAS, Krasnoyarsk, 660036, Russia

ARTICLE INFO

Keywords:
Rare-earth cobalt oxides
Crystal structure
Thermoelectric properties
Mechanical activation

ABSTRACT

Background: Crystal structure of rare-earth $LaCoO_3$ cobalt oxide subjected to high energy mechanical activation has been studied. In the temperature range of 300–800 K, the electrical conductivity and Seebeck coefficient were measured. Thermal conductivity was measured at 300–480 K.
Methods: Comparative analysis of thermoelectric properties of the samples prepared by standard solid-state reaction and using high-energy mechanical activation was carried out.
Findings: It was found that the experimental X-ray diffraction patterns are best described within the model that allows the coexistence of two domains in samples with the same crystal symmetry, but different lattice a and c parameters. The percentage ratio of these domains in the samples depends significantly on the size of the initial particles in the solid-state synthesis reaction and the annealing temperature. Mechanical activation and increase of synthesis temperature result in change of Seebeck coefficient sign and significant decrease of electrical resistivity. The Seebeck coefficient of non-activated samples takes positive values over the entire temperature range and decreases monotonically with increasing temperature, in contrast to mechanically activated samples exhibiting ambipolar behavior.

1. Introduction

Unusual physical properties, along with the practical application possibility, are the reason for the active long-term research of rare-earth $LnCoO_3$ (Ln = La, rare-earth metal) cobalt oxides [1,2]. The Co^{3+} ion finding possibility in different low (LS, S = 0), intermediate (IS, S = 1) and high (HS, S = 2) spin states, which is the reason for the unique magnetic [3,4], transport [5] and thermodynamic [6] properties are the main feature of this compounds. The crystal structure of bulk samples is rhombohedral $R\bar{3}c$ perovskite type for $LaCoO_3$ [7] and orthorhombic $Pbnm$ for other $LnCoO_3$ with rare earth cations of smaller ionic radius [6,8]. The rare-earth Ln^{3+} ions are surrounded by a slightly distorted cuboctahedron consisting of 12 oxygen ions, and the cobalt ions form octahedral CoO_6 complexes.

The series basic representative for which magnetic and transport anomalies are most pronounced is rare-earth $LaCoO_3$ cobaltite. Despite the seemingly comprehensive research, new information about its properties appears regularly. In the study of $LaCoO_3$ in ultrastrong magnetic fields up to 600 T at various temperatures, an unusual magnetostriction field dependence was obtained [9]. Based on an integrated study of the magnetic susceptibility, specific heat, and thermal expansion of a single crystal $LaCoO_3$ free of cobalt and oxygen vacancies, a consistent interpretation of strongly correlated spin state and crystal lattice for the pseudo-cubic $LaCoO_3$ perovskite proposed in [10]. It was found in [11,12] that with a decrease in the rare-earth element ionic radius, the samples oxygen nonstoichiometry increases, and the perovskites thermodynamic stability decreases. Research to study the samples properties under the influence of hydrostatic and chemical pressure [13] and the application possibilities [14] is being carried out. The high Seebeck coefficient [15,16], the absence of toxic elements, resistance to oxidizing environments, and the various substitutions possibility in rare-earth cobalt oxides make it possible to consider them as potential thermoelectric materials [17]. Among the oxide materials, cobalt-based systems ($LaCoO_3$ [18–20], $Ca_3Co_4O_9$ [21,22], Na_xCoO_2 [23,24]) are promising for thermoelectric applications because of the co-existence of several charges states and its different spin-states [20,25] what

* Correspondence to: Kirensky Institute of Physics KSC SB RAS, Krasnoyarsk, 660036, Russia.
E-mail address: orlov@iph.krasn.ru (Y.S. Orlov).

https://doi.org/10.1016/j.jtice.2024.105560
Received 26 February 2024; Received in revised form 21 April 2024; Accepted 15 May 2024
Available online 28 May 2024

promises to decouple thermoelectric parameters using the high-entropy concept in several materials. The random distribution of cations at the rare-earth site results in a significant lowering of phonon thermal conductivity k_{ph}. As a result, a maximum figure of merit (ZT) of 0.23 is obtained at 350 K for $(LaNdPrSmEu)_{0.95}Sr_{0.05}CoO_3$, which is one of the highest values of ZT reported at this temperature for oxide materials [26]. An improvement in ZT is obtained in several cobalt-oxide composites, viz. $Ca_3Co_4O_9$/Ag [27], $LaCoO_3$/graphene [28], $LaCoO_3/La_{0.7}Sr_{0.3}MnO_3$ [29], $LaCoO_3/La_{0.7}Sr_{0.3}CoO_3$ [30,31]. The simultaneous optimization of electrical and thermal transport in an acoustically mismatched composite oxide that consists of $La_{0.95}Sr_{0.05}Co_{0.95}Mn_{0.05}O_3$ and highly conducting WC (with different elastic properties than $La_{0.95}Sr_{0.05}Co_{0.95}Mn_{0.05}O_3$) proposed in [32]. Synergistic effect of improved electrical σ and lowered thermal k_{ph} conductivity results in improved thermoelectric figure of merit (ZT) of 0.20 at 463 K for $(1-x)La_{0.95}Sr_{0.05}Co_{0.95}Mn_{0.05}O_3/(x)$WC composite [32].

Since the ground state in bulk $LnCoO_3$ cobaltites is the nonmagnetic LS state, an additional impetus to intensify research has recently been the discovery of ferromagnetic ordering in epitaxial films [33], nanoparticles [34,35], nanowires [36], and on the $LaCoO_3$ single crystals surface [37].

To date, a number of methods for the nanostructured LnCoO3 synthesis, including the sol–gel method [38–40], coprecipitation [41, 42], hydrothermal method [43,44], electrochemical oxidation [45], mechanochemical activation in planetary ball mills [46,47], and others have been proposed. Each method has its own advantages and disadvantages associated with chemical homogeneity, environmental friendliness and ease of synthesis, the rate of the final product formation and the raw materials cost. At the same time, the synthesis methods and modes significantly affect the final product properties.

In this work, we study (i) the morphology, structural, and thermoelectric properties of rare-earth $LaCoO_3$ cobalt oxides synthesized both by the standard ceramic technology and from nanoparticles obtained by high-energy grinding of cobaltite in a ball micromill and (ii) influence of annealing temperature on these properties. The decrease of the size of initial particles and increase of annealing temperature result in significant reduction of electrical resistivity, Seebeck coefficient sign change, and improvement of the thermoelectric figure of merit.

2. Experimental

At the initial stage, according to the standard ceramic technology, high-purity oxides Co_3O_4 (99.7%, metals basis) and La_2O_3 (99.99%, REO; pre-drying at 1223 K for 6 h), taken in a stoichiometric amount, were thoroughly mixed in an agate mortar using ethanol, annealed in air at 1373 K for 24 h and cooled together with the furnace to room temperature at a rate of 2 deg/min. After annealing, the resulting mixture was grinded, pressed into tablets, which were annealed in air at 1373 K for 16 h with intermediate grinding – pressing – calcination (LCO-1373 sample). To obtain samples with a nanometer size initial particles (LCO(m) samples) high-energy grinding (mechanoactivation) was used in a Pulverisette 7 premium line planetary micromill (Fritsch GmbH, Germany). LCO-1373 tablets, grinded in an agate mortar, were loaded into a tungsten carbide grinding jar and were grinded by balls 3 mm in diameter. The total grinding time was 60 minutes. To prevent particles from sticking together during grinding, <<wet>> grinding in ethanol was used. After evaporation, the resulting mechanically activated nanopowder was pressed into disks 20 mm in diameter, which were annealed in air at 1023 K (LCO(m)-1023), 1223 K (LCO(m)-1223) and 1373 K (LCO(m)-1373). Synthesis process schematic representation is shown in Fig. 1. To measure the electrical resistance and the Seebeck coefficient, bars of $5 \times 13 \times 1$ mm^3 were cut from the annealed disks.

Powder X-ray diffraction (PXRD) data were acquired on a PANalyticalX'Pert PRO diffractometer equipped with a PIXcel solid-state detector using CoKα radiation in the 2θ 10–150° range. Powder samples were prepared by octane grinding of finished bars in an agate mortar and packed in a flat sample holder for PXRD measurements in Bragg–Brentano geometry. Full profile PXRD refinement was performed using Derivative Difference Minimization (DDM) [48].

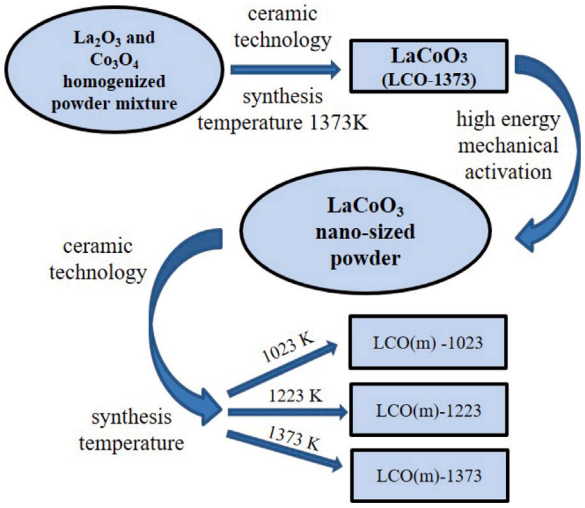

Fig. 1. Synthesis process scheme.

To visualize the surface morphology and samples crystallinity degree, a JEOL JEM-2100 transmission electron microscope and a JEOL JSM-7001F scanning electron microscope was used. Annealed samples density was determined on an analytical balance Mettler Toledo XP205 (Switzerland) with an attachment for hydrostatic weighing. The measurements were carried out in ethanol.

Temperature dependences of Seebeck coefficient and electrical resistivity were obtained on an original home-made experimental setup (similar to [49]) in air at the L.V. Kirensky Institute of Physics SB RAS. SiGe was used as a reference, the relative error was 2% and 5% in measuring of the resistivity and the Seebeck coefficient respectively. The thermal conductivity was measured on an IT-λ-400 thermal conductivity meter.

All measurements were performed on freshly prepared samples.

3. Results and discussion

3.1. Crystal structure analysis

Most neutron or X-ray diffraction data describe the $LaCoO_3$ space group as $R\bar{3}c$, although $LaCoO_3$ structure monoclinic distortion ($I2/a$ space group) was observed in [50], which was associated with Co^{3+} ionic radius increasing from 0.545 Å in the LS state to 0.61 Å in the HS state and CoO_6 octahedral Jahn–Teller (JT) distortion arising [6]. It was shown in [51] that the structure of nanosized $LaCoO_3$ can be interpreted both in terms of the $R\bar{3}c$ and $I2/a$ space group. As the temperature increases, the value of the JT parameter increases and reaches 6% at room temperature [50].

X-ray diffraction analysis did not reveal the presence of impurities and unreacted initial oxides residues in our samples. For all samples, X-ray diffraction patterns showed only peaks corresponding to the standard $LaCoO_3$ perovskite powder diffraction pattern with rhombohedral symmetry $R\bar{3}c$ space group, which is consistent with extensive literature data [7,8,35,38,52].

X-ray diffraction patterns refinement by the Rietveld method using DDM (Fig. 2a) showed that under the single-phase samples composition assumption, it is not possible to completely describe the experimental profile, which is clearly manifested in the difference curve (Fig. 2a, inset). The difference is more pronounced for mechanically activated LCO(m) samples and relatively small for LCO-1373.

Table 1
$LaCoO_3$ samples rhombohedral ($R\bar{3}c$) lattice parameters at 298 K in the <<two modifications>> model.

Modification	Parameter	Sample			
		LCO-1373	LCO-1373 (T = 773 K)[a]	LCO(m)-1023	LCO(m)-1373
1	a, Å	5.44369(3)	5.49649(7)	5.4450(3)	5.4530(2)
	c, Å	13.09327(6)	13.2965(1)	13.100(2)	13.1159(3)
	V, Å^3	336.020(4)	347.888(9)	336.35(5)	337.75(2)
	c/a	2.4052	2.4191	2.4059	2.4053
	%	93	92	66	84
2	a, Å	5.435(3)	5.491(2)	5.430(3)	5.4390(7)
	c, Å	13.171(10)	13.359(17)	13.176(7)	13.174(6)
	V, Å^3	337.0(5)	348.8(5)	336.5(4)	337.6(2)
	c/a	2.423	2.433	2.427	2.422
	%	7.0 ± 0.5	8	34	16

[a] Powder X-ray diffraction data were acquired at 773 K

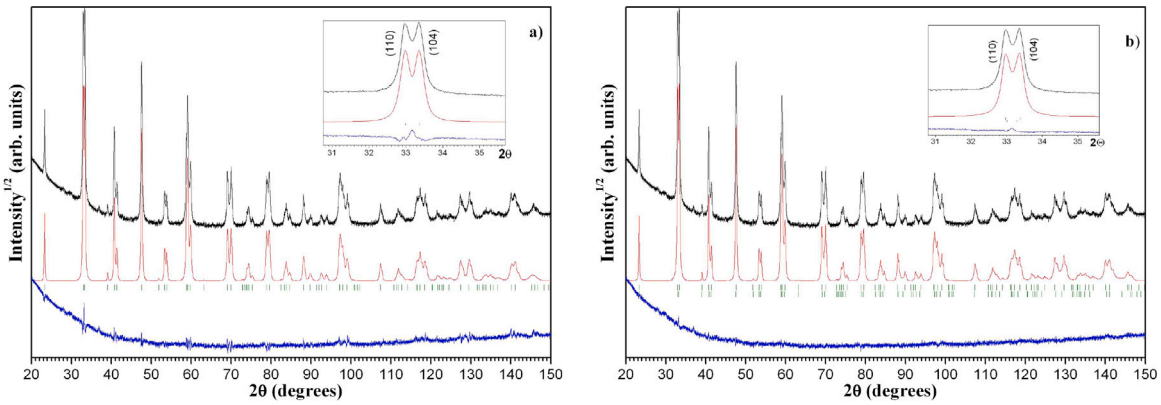

Fig. 2. LCO(m)-1023 sample experimental (black), calculated (red), and difference (blue) X-ray pattern at T = 298 K. Calculated reflections positions are shown by dashes. (a) single phase model; (b) two modifications coexistence model with the same crystal symmetry but different lattice parameters. The inset is an X-ray diffraction pattern enlarged fragment in the region of the (110) and (104) reflections. (For interpretation of the references to color in this figure legend, the reader is referred to the web version of this article.)

It is considered that the impulsive impact nature during mechanochemical activation has a local character, i.e. during processing the stress field does not arise in the entire volume of a solid particle, but only at its contact with another particle or working fluid. Accordingly, it can be assumed that, even with a small particle size, both the main phase and the surface layers' material transformation under the influence of treatment can be observed in the activated material. It is reasonable to assume that the observed differences (Fig. 2a, difference curve) reflect changes in part of the crystal structure that occur during mechanical activation. Subsequent high-temperature annealing provides partial relaxation of the induced changes, but does not lead to the structure return to its original state even at treatment temperatures of 1023–1373 K, which ultimately makes it difficult to describe the structure within the framework of a single-modification approach.

For a correct description of X-ray diffraction patterns, a second component (modification) with the same structure but different lattice parameters was introduced. The results of full-profile PXRD refinement under the two modifications presence assumption for LCO(m)-1023 are shown in Fig. 2b, and the LCO-1373, LCO(m)-1023 and LCO(m)-1373 samples crystal lattice parameters in Table 1 and Fig. 3.

It can be seen from the given data that unit cell parameter a of the second modification is systematically less than that of the first modification, in contrast to the parameter c, which is systematically higher (Table 1, Fig. 3), while the ratio c/a within the error does not depend on the activation procedure and heat treatment and is equal to 2.4055 ± 0.0009 and 2.424 ± 0.006 for modifications << 1>> and << 2>>, respectively. Maximum fraction of the second modification is observed in the mechanically activated LCO(m)-1023 sample; heating at 1373 K results in its twofold decrease (LCO(m)-1373 sample). Interestingly, that the LCO-1100 sample, which was not subjected to intensive mechanical activation, also contains a small but reliably identifiable amount of the second modification (7%).

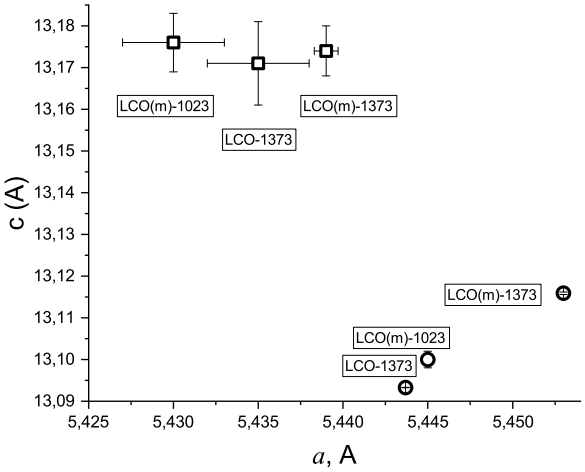

Fig. 3. a and c crystal lattice parameters interconnection of the 1st (○) and 2nd (□) $LaCoO_3$ modifications present in LCO-1373, LCO(m)-1023 and LCO(m)-1373. Whiskers correspond to the standard deviation (SD) of a and c parameters, the SD values for the 1st modification are smaller than the marker size.

Fig. 4 shows the crystal structure of rhombohedral $LaCoO_3$ ($R\bar{3}c$ symmetry at room temperature). The structure is valid for both components (modifications). The structural difference between the modifications is demonstrated by slight expansion of the lattice in the c-direction with simultaneous shrinkage along a and b axes.

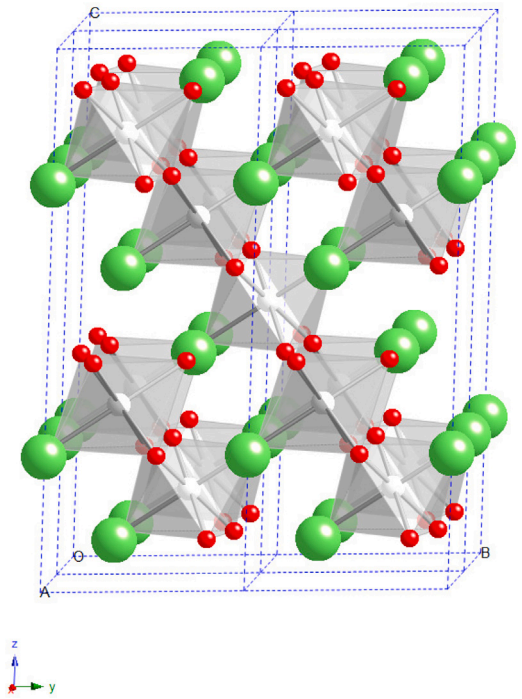

Fig. 4. Structure of $LaCoO_3$. Gray octahedra represent Co^{3+}, green spheres represent La^{3+} and red spheres are oxygen. Color online.

The heating of the samples up to 500° C (using LCO-1373 as an example, Table 1) leads to the significant increase of unit cell volume originating from both thermal and anomalous thermal $LaCoO_3$ expansion near the insulator–metal transition temperature [5,52,53], but has almost no effect on the second modification content.

So, the presence of two components of $LaCoO_3$ crystal lattice we consider as a surface effect. It is known that the surface properties (structure, chemical composition, etc.) of various objects (crystals, nanoparticles, ceramic grains, films, etc.) can differ significantly from the bulk ones. In our case, the LCO(m)-1023 sample, in addition to large poorly interconnected ceramic grains, contains nanoparticles up to 100 nm in size (Fig. 6b). A large number of stresses, and distortions are possible on the surface of such particles. The ratio of surface to volume properties in the LCO(m)-1023 sample is maximal, which leads to the higher content of the second crystal lattice modification (Table 1).

3.2. Samples morphology

Fig. 5 shows LCO(m) powder micrographs obtained as a result of LCO-1373 formed bulk perovskite high-energy wet milling. High-resolution transmission electron microscopy (HRTEM) image (Fig. 5a) confirms the nanometer size of the obtained particles. The absence of a clear faceting (Fig. 5a) indicates that these particles are agglomerates formed from smaller particles during alcohol evaporation. At the same time, larger grains with a clear cut (Fig. 5b), with sizes exceeding 100 nanometers, are also found in the evaporated powder composition, which is associated either with insufficient grinding time or with sticking of grains on the grinding jar surface.

Scanning electron microscopy (SEM) images of sintered sample surfaces (Fig. 6) demonstrate the external similarity of LCO-1373 and LCO(m)-1373 particles, which are close to spherical, that was also observed in [47,51]. At the same calcination temperatures, the grain size of mechanically activated LCO(m)-1373 (Fig. 6c) is smaller than that of LCO-1373 (Fig. 6a) and the sintering necks are more pronounced. LCO(m)-1023 (Fig. 6b) is characterized by a large number of pores, an uneven distribution of particles, and weak sintering.

Experimental density and samples porosity calculating results, based on two crystal structure modifications average volume V_{av} (Table 2), are in good agreement with the morphology of the samples. Theoretical density was calculated using the formula $\rho_{theor} = M/V_M$, were M is molar mass and $V_M = (V_{cell} \cdot N_A)/Z$ ($V_{cell} = V_{av}$, N_A – Avogadro constant, $Z = 6$). The maximum density is observed for LCO(m)-1373. The LCO(m)-1023 sample porosity is more than twice that of LCO(m)-1373.

According to energy dispersive spectroscopy (EDS) analysis, the composition of all samples is close to $LaCoO_3$.

3.3. Thermoelectric properties

3.3.1. Electrical conductivity

Temperature dependences of electrical resistivity $\rho(T)$ qualitatively correspond to the semiconductor conductivity type $d\rho/dT < 0$ over the entire considered temperature range from 300 to 800 K (Fig. 7a). In consistent with the results of [51], which show that bulk sample electrical resistivity is lower than that of a nanostructured, in our case, the maximum resistivity is observed in the LCO(m)-1023 sample obtained from nanosized particles and obtained at a lower annealing temperature compared to LCO(m)-1373. The electrical resistance of the samples rapidly decreases with increasing temperature up to a temperature corresponding to the semiconductor–metal transition near 500 K. Above this temperature, the graphic dependences flatten out.

The temperature dependence are shown in Fig. 7b and are in good agreement with those obtained in [5,54–57]. Neither the sample preparation procedure nor the annealing temperature affect the insulator–metal transition (IMT) temperature, marked in Fig. 7b by a straight vertical line corresponding to 490 K. Therefore, it can be argued that IMT transition is associated with intrinsic electronic structure changes. In [58], we have showed that the IMT is due to the attenuation of electron correlations with increasing of the HS state population.

3.3.2. Seebeck coefficient

Seebeck coefficient $S(T)$ temperature dependences in the temperature range 300–800 K are shown in Fig. 8a. LCO-1373 sample, which was not subjected to mechanical activation, is characterized by the classical dependence $S(T)$ with a high absolute value of $S = 477$ μV/K) at room temperature, followed by a gradual decrease with increasing temperature [15,59,60].

For LCO(m)-1023, a maximum is observed, and LCO(m)-1223 and LCO(m)-1373 samples demonstrate transition from negative Seebeck coefficient values to the region of positive ones. In this case, Seebeck coefficient sign change temperature shifts to higher temperatures (370 K for LCO(m)-1023 and 410 K for LCO(m)-1373). The possibility of S negative value in the temperature range below room temperature was paid attention to in early works [61]. Negative values were also observed for $Gd_{1-x}Sr_xCoO_{3-\delta}$ [62], $LaCo_{1-x}Ti_xO_3$ [60], and $RBaCo2O_{5+x}$ (R = Gd, Nd) [63] compounds, where the change of Seebeck coefficient sign was associated with oxygen nonstoichiometry change. For undoped rare-earth cobalt oxides or in the case of isovalent substitution, negative S values are quite rare [57,64,65] and are usually associated with impurities that introduce additional electron carriers or with low substitution in the A or B crystal structure positions [60,66]. $S(T)$ sign change indicates that two types of carriers are present in $LaCoO_3$, which are dominant in different temperature ranges.

Temperature dependences of thermoelectric power factor $PF(T)$ show a flattening at 650 K, that are most clearly seen for LCO(m)-1223 and LCO(m)-1373. Seebeck coefficient coincidence at temperatures above 600 K within the measurement error and higher LCO(m)-1373 sample conductivity result in 2.5-fold higher thermoelectric power factor PF (Fig. 8b) of the mechanically activated sample compared to the LCO-1373 sample.

In contrast to LCO-1373 sample, LCO(m)-1373 sample changes the Seebeck coefficient sign with increasing temperature (Fig. 8a). Below

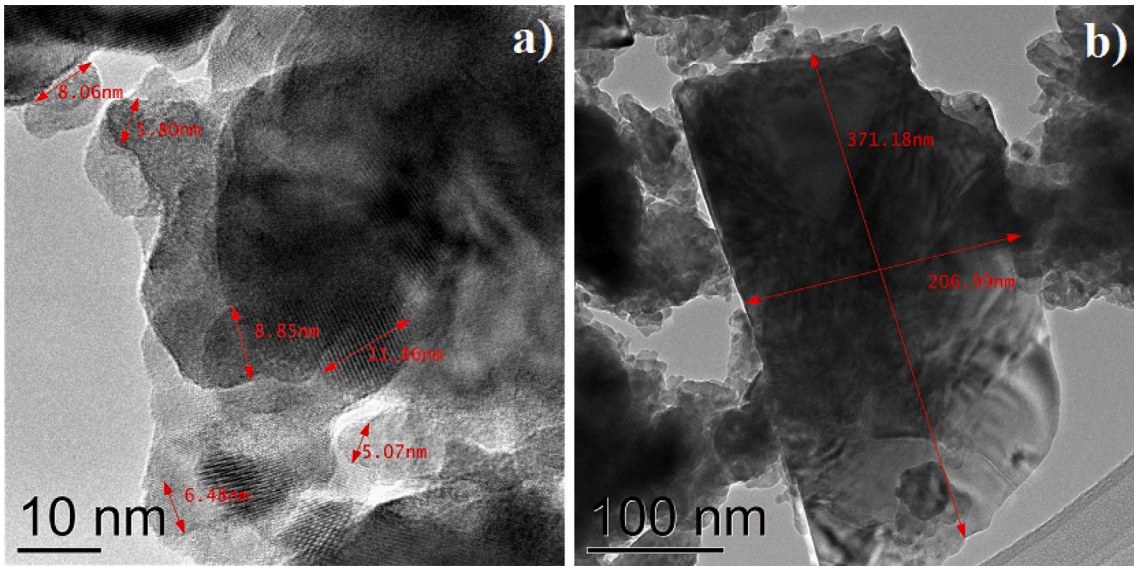

Fig. 5. HRTEM (a) and TEM (b) images of the $LaCoO_3$ nanopowders after high-energy LCO-1373 perovskite wet milling, evaporation and disaggregation in an ultrasonic bath.

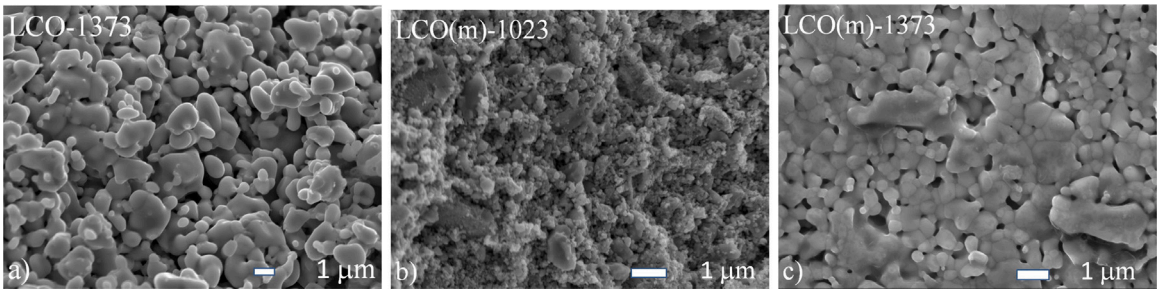

Fig. 6. SEM images of the $LaCoO_3$ samples surfaces: $LaCoO_3$ annealed at 1373 K (a); mechanically activated $LaCoO_3$ annealed at 1023 K (b), and at 1373 K (c).

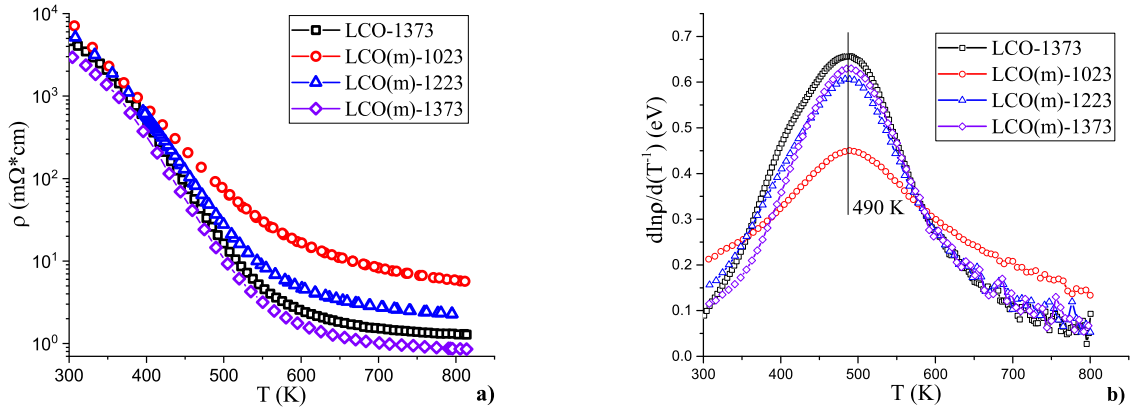

Fig. 7. Electrical resistivity $\rho(T)$ (a) and $d\ln\rho/d\left(k_BT\right)^{-1}$ (b) temperature dependences. The vertical line in the Fig. (b) corresponds to the insulator–metal transition temperature.

Table 2
Average V_{av} volume, theoretical ρ_{theor} and experimental ρ_{exp} densities, $LaCoO_3$ samples relative density and porosity depending on sample preparation and annealing temperature.

Notation	V_{av}	ρ_{theor} (g/cm^3)	ρ_{exp} (g/cm^3)	Density ratio (%)	Porosity (%)
LCO-1373	336.092(5)	7.290	6.708	92.01	7.99
LCO(m)-1023	336.417(9)	7.283	6.251	85.83	14.17
LCO(m)-1373	337.730(9)	7.255	6.793	93.63	6.97

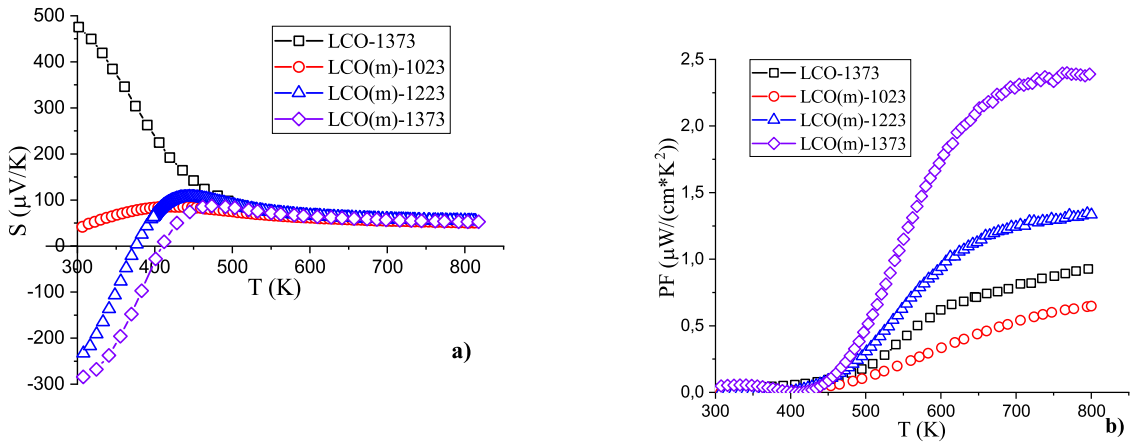

Fig. 8. $LaCoO_3$ Seebeck coefficient $S(T)$ (a) and thermoelectric power factor PF (b) temperature dependences for samples with different preparation and annealing temperature.

we present qualitative arguments that allow us to understand this feature.

In the Boltzmann transport theory, the electrical conductivity, σ, and Seebeck coefficient, S, are expressed as:

$$\sigma_{ij}(\mu,T)=\int_{-\infty}^{+\infty}\sigma_{ij}(\varepsilon)\left(-\frac{\partial f_F(\varepsilon,\mu,T)}{\partial\varepsilon}\right)d\varepsilon, \tag{1}$$

$$[\sigma S]_{ij}(\mu,T)=\frac{1}{eT}\int_{-\infty}^{+\infty}(\varepsilon-\mu)\,\sigma_{ij}(\varepsilon)\left(-\frac{\partial f_F(\varepsilon,\mu,T)}{\partial\varepsilon}\right)d\varepsilon, \tag{2}$$

where

$$\sigma_{ij}(\varepsilon)=e^2\sum_{\lambda}\int\frac{d\boldsymbol{k}}{4\pi^3}\tau_\lambda(\boldsymbol{k})\,v_{i,\lambda}(\boldsymbol{k})\,v_{j,\lambda}(\boldsymbol{k})\,\delta\left(\varepsilon-\varepsilon_\lambda(\boldsymbol{k})\right) \tag{3}$$

is the energy-dependent conductivity, and $f_F(\varepsilon,\mu,T)=\frac{1}{e^{\varepsilon-\mu/k_BT}+1}$ is the Fermi–Dirac distribution function. These equations are known as the Mott relations. In Eq. (3) $\varepsilon_\lambda(\boldsymbol{k})$ is the band energy at $\boldsymbol{k}$- point (λ – band index); $\boldsymbol{v}_\lambda(\boldsymbol{k})=\hbar^{-1}\nabla_k\varepsilon_\lambda(\boldsymbol{k})$ ($v_{i,\lambda}(\boldsymbol{k})=\hbar^{-1}\partial\varepsilon_\lambda(\boldsymbol{k})/\partial k_i$) is the group velocity; $\tau_\lambda(\boldsymbol{k})$ is the relaxation time due to scattering with phonons and/or disorders/impurities. For an isotropic medium or crystals with a symmetry close to cubic $\sigma_{ij}(\varepsilon)=\sigma(\varepsilon)\delta_{ij}$ and $\sigma_{ij}(\mu,T)=\sigma(\mu,T)\delta_{ij}$, where δ_{ij} is Kronecker delta function. In this case, instead of Eq. (2) we have

$$S(\mu,T)=-\frac{1}{e\sigma T}\int_{-\infty}^{+\infty}(\varepsilon-\mu)\,\sigma(\varepsilon)\left(-\frac{\partial f_F(\varepsilon,\mu,T)}{\partial\varepsilon}\right)d\varepsilon. \tag{4}$$

The formulae above can be simplified in a couple of important limiting cases. In metals, semimetals and degenerate semiconductors, where transport only occurs near the Fermi level and $\sigma(\varepsilon)$ changes slowly in the range $\varepsilon\approx\mu\pm k_BT$, one can perform a Sommerfeld expansion $\sigma(\varepsilon)=\sigma(\mu)+\sigma'(\mu)(\varepsilon-\mu)+O\left[(\varepsilon-\mu)^2\right]$, which leads to

$$S(\mu,T)=-\frac{\pi^2k_B^2T}{3e}\left.\frac{d\ln\sigma(\varepsilon)}{d\varepsilon}\right|_{\varepsilon=\mu}. \tag{5}$$

This expression is sometimes called “the Mott formula”, however it is much less general than Mott’s original formula expressed above. In semiconductors at low levels of doping (less than degeneracy level), transport only occurs far away from the Fermi level. At low doping in the conduction band (where $\varepsilon_C-\mu>>k_BT$, ε_C is the minimum energy of the conduction band edge), one has $-\frac{\partial f_F(\varepsilon)}{\partial\varepsilon}\approx\frac{1}{k_BT}e^{-(\varepsilon-\mu)/k_BT}$. Approximating the conduction band levels’ conductivity function as $\sigma(\varepsilon)=A_C\left(\varepsilon-\varepsilon_C\right)^{a_C}$ for some constants A_C and a_C,

$$S_C=-\frac{k_B}{e}\left[\frac{\varepsilon_C-\mu}{k_BT}+a_C+1\right], \tag{6a}$$

$$\sigma_C=A_C\left(k_BT\right)^{a_C}e^{-\frac{\varepsilon_C-\mu}{k_BT}}\Gamma\left(a_C+1\right). \tag{6b}$$

Whereas in the valence band when $\mu-\varepsilon_V>>k_BT$ and $\sigma(\varepsilon)=A_V\left(\varepsilon_V-\varepsilon\right)^{a_V}$

$$S_V=\frac{k_B}{e}\left[\frac{\mu-\varepsilon_V}{k_BT}+a_V+1\right], \tag{7a}$$

$$\sigma_V=A_V\left(k_BT\right)^{a_V}e^{-\frac{\mu-\varepsilon_V}{k_BT}}\Gamma\left(a_V+1\right). \tag{7b}$$

The values of a_C and a_V depend on material details; in bulk semiconductor these constants range between 1 and 3.

In general, however the semiconductor may also be intrinsic in which case the bands conduct in parallel (both valence band and conduction band contribute to transport), and so the measured (effective) values will be

$$S=\frac{\sigma_CS_C+\sigma_VS_V}{\sigma}, \tag{8a}$$

$$\sigma=\sigma_C+\sigma_V. \tag{8b}$$

In extrinsic (doped) semiconductors either the conduction or valence band will dominate transport, and so one of the numbers above will give the measured values.

The ground state of $LaCoO_3$ is a nonmagnetic insulator with a lowspin (LS, S = 0) state of the Co^{3+} ion with t_{2g}^6 electronic configuration in the crystal field of the O_6 octahedron. A transition to the paramagnetic state occurs in the vicinity of $T=100$ K, which is evident from the sharp increase in the magnetic susceptibility. However, the spin state of Co^{3+} ions above $T=100$ K remains a mystery for a long time. According to the Tanabe–Sugano diagrams, for the d^6-ion with a change in the crystal field, a crossover between the LS and HS terms is possible. In the framework of the standard model of an ion in a crystal field, the energy of the IS state is so much higher than that for the LS and HS states that thermal population of it is out of the question. Numerous and most modern studies have not yet provided unambiguous evidence in favor of the realization of the IS or HS state in the intermediate temperature range. We will provide references to works that are quite important in our opinion in favor of the IS- [7,67–70] and HS- [71–76] states. In our works and in this one, we adhere to the scenario in which the HS state acts as the first excited state. In our opinion, this particular scenario is the most attractive lately.

In stoichiometric $LaCoO_3$ we assume that the Co ion is in the state $3d^6$. At 0 K it is expected that this substance will be an insulator. Conductivity can arise, however, at finite temperatures by the removal of an electron from one Co ion, and placing it on another Co ion at a large distance. This is, of course, equivalent to the simultaneous formation of Co^{2+} and Co^{4+} ions or $Co^{3+}\underline{L}$ configuration, where $\underline{L}$ is a ligand’s (oxygen) hole spectroscopic notation. If an energy E_g is

required to create such pairs, we may expect a conductivity of the form $e^{-E_g/2k_BT}$. Thus we might at first be tempted to attribute the anomaly at 500 K to just such an intrinsic behavior. (It is not difficult to envisage a change in magnetic moment in the transition $2Co^{3+} \rightarrow Co^{2+} + Co^{4+}$ or $Co^{3+}\underline{L}$.) That the situation is not so simple is easily seen. One observes that if the conductivity is written in the form

$$\sigma = N_c e\eta e^{-E_g/2k_BT}, \tag{9}$$

where N_c, is essentially the density of states and η is the mobility, the extrapolation of σ to $1/T = 0$ gives us the product $N_c e\eta$. Since N_c, cannot be sensibly greater than 10^{22}, the experimental conductivity data above the transition temperature indicate that η would to be of the order of 10^4 $cm^2/(V\,s)$ in order for this explanation to be valid. Such a mobility is pretty much out of the question [15].

The substantial difference between the spin gap and the electrical conduction activation energy $E_a \approx 0.1$ eV ($E_g = 2E_a$) for low temperatures implies that $LaCoO_3$ is not a simple band insulator [77]. Moreover, a considerable difference between charge gap $2E_a \approx 2300$ K and the temperature $T_{IMT} \approx 500$ K of the insulator–metal transition indicates that the latter can hardly be explained in the model of a narrow-gap semiconductor [5]. Therefore, we conclude that the energy E_g must be temperature dependent.

We have shown in [58,78] that the spin crossover in $LaCoO_3$ changes the Mott–Hubbard energy gap

$$U(d^n) = E\left(d^{n-1}\right) + E\left(d^{n+1}\right) - 2E(d^n) \tag{10}$$

[79] and results in the gap energy $E_g(T)$ decrease with increasing temperature and an insulator–metal transition at $T_{IMT} \approx 500$ K. In stoichiometric $LaCoO_3$, $t_{2g}^6\left({}^1A_{1g}, Co^{3+}\right) \rightarrow t_{2g}^6 e_g^1\left({}^2E_g, Co^{2+}\right)$ and $t_{2g}^6\left({}^1A_{1g}, Co^{3+}\right) \rightarrow t_{2g}^6\underline{L}\left({}^1A_{1g}\underline{L}, Co^{3+}\underline{L}\right)$ electronic transitions at $T = 0$ K determine respectively the narrow conduction band (CB) and the wide valence band (VB), formed mainly by the oxygen $2p$ states, mass center position. The $LaCoO_3$ band structure at low temperatures is the charge transfer insulator type with a band gap of 0.2 eV and a chemical potential μ near the top of VB (Fig. 9a). According to Eq. (10), for the LS-state we have

$$U_{LS} = E_{{}^1A_{1g}\underline{L}}\left(t_{2g}^6\underline{L}, Co^{3+}\underline{L}\right) + E_{{}^2E_g}\left(t_{2g}^6 e_g^1, Co^{2+}\right) - 2E_{{}^1A_{1g}}\left(t_{2g}^6, Co^{3+}\right). \tag{11}$$

As the temperature increases, the Co^{3+} ions HS state thermal population occurs. In addition to the electronic transitions discussed above, $t_{2g}^4 e_g^2\left({}^5T_{2g}, Co^{3+}\right) \rightarrow t_{2g}^5 e_g^2\left({}^4T_{1g}, Co^{2+}\right)$ and $t_{2g}^4 e_g^2\left({}^5T_{2g}, Co^{3+}\right) \rightarrow t_{2g}^4 e_g^2\underline{L}\left({}^5T_{2g}\underline{L}, Co^{3+}\underline{L}\right)$ transitions, which form new CB and O$2p$ VB mass center position respectively (Fig. 9b), begin to play an important role. For the HS state, according to Eq. (10)

$$U_{HS} = E_{{}^5T_{2g}\underline{L}}\left(t_{2g}^4 e_g^2\underline{L}, Co^{3+}\underline{L}\right) + E_{{}^4T_{1g}}\left(t_{2g}^5 e_g^2, Co^{2+}\right) - 2E_{{}^5T_{2g}}\left(t_{2g}^4 e_g^2, Co^{3+}\right). \tag{12}$$

$U_{HS} \ll U_{LS}$ and at $T_{IMT} \approx 500$ K the dielectric gap E_g vanishes. The VB and CB begin to overlap, as in semimetal (Fig. 9c).

Stoichiometric $LaCoO_3$ electronic structure schematically shown in Fig. 9a-c explains the Seebeck coefficient temperature dependence of the LCO-1373 sample. This phenomenon can be explained by Eq. (8). In this case at low T, Eq. (8)a is simplified to $S \approx S_V$ because of $\sigma_V/\sigma \gg \sigma_C/\sigma$. These can be understood from two aspects: (1) the term of $\partial f_F\left(\varepsilon_k\right)/\partial\varepsilon_k$ in CB is vanishingly small because of the large enough bandgap (0.2 eV) (Fig. 9a). (2) The large bandgap also makes thermal activation from VB to CB impossible. So, there is hardly any electrons in CB. With increasing temperature, the band gap E_g decreases (Fig. 9b), but the contribution of the valence band, due to its larger width and higher current carriers mobility (lower effective mass) in it, remains dominant and, according to Eq. (7)a, at $T < T_{IMT}$, the Seebeck coefficient monotonically decreases from high values with increasing T. At T_{IMT} $LaCoO_3$ transforms into a semimetal state (Fig. 9c), and we observe a linear temperature dependence of $S(T)$ at $T > T_{IMT}$ (Fig. 8a) according to Eq. (5).

According to our thermogravimetric measurements, the oxygen nonstoichiometry δ of all samples does not exceed 0.01 (3% of the oxygen nominal). The presence of δ leads to electron self-doping (Co^{2+} ions appearance). As shown in [59], even a minor (< 0.5%) substitution of cobalt or lanthanum ions for titanium and cerium ions respectively (electron doping) result in Seebeck coefficient sign change. The Seebeck coefficient becomes negative (n-type). Apparently, of all the samples, LCO(m)-1373 contains the least amount of oxygen and is the most nonstoichiometric, which, as in the case of electron doping, leads to negative Seebeck coefficient values at low temperatures (Fig. 8a). Figs. 9d–f schematically shows the LCO(m)-1373 sample electronic structure temperature dependence, which qualitatively explain it Seebeck coefficient sign change with increasing temperature (Fig. 8a).

At low temperatures, the chemical potential μ of LCO(m)-1373, in contrast to LCO-1373 (Fig. 9a), lies near the bottom of the conduction band (Fig. 9d). At very low T, Eq. (8)a is simplified to $S \approx S_C$ because of $\sigma_V/\sigma \ll \sigma_C/\sigma$, so only CB participates in the transport. As T increases, σ_V/σ and σ_C/σ get close. So, the transport behavior is determined by CB (metallic model behavior) and VB (semiconductor model behavior) together. As T continues to rise, $E_g(T)$ decreases (Fig. 9e), σ_V/σ and σ_C/σ get closer, even $\sigma_V/\sigma \sim \sigma_C/\sigma$, and $S_V > S_C$, according to Eq. (8)a, the sign of S becomes positive, leading to an exotic ambipolar behavior, namely, at relatively low-temperature range, negative S nonmonotonically changes with increasing T, and at high T, the sign of S changes, shown in Fig. 8a. A similar Seebeck coefficient ambipolar behavior in organic thermoelectric materials was discussed in [80]. The large σ_V at high T is attributed to thermal activation, and the thermal activation is attributed to a small bandgap $E_g(T)$ (Fig. 9e). At T_{IMT} LCO(m)-1373 transforms into a semimetal state (Fig. 9f), and we observe, as in the case of LCO-1373, $S(T)$ linear temperature dependence at $T > T_{IMT}$ (Fig. 8a) according to Eq. (5). At $T > T_{IMT}$, the Seebeck coefficients of all samples coincide (Fig. 8a) and linearly decrease. Using the generalized Heikes formula for the Seebeck coefficient proposed in [23] for cobalt oxides, one can estimate the $S(T)$ limiting value at $T \rightarrow \infty$. According to [59], $S = -35$ μV/K.

From the above, the fundamental importance of oxygen nonstoichiometry control becomes clear. For example, recently in [10] a fully stoichiometric free from cobalt and oxygen vacancies $LaCoO_3$ single crystal was obtained. Its study has brought greater understanding of rare earth cobalt oxides' physics.

3.3.3. Thermal conductivity

LCO(m)-1023 and LCO(m)-1373 samples thermal conductivity was measured in the temperature range 300–480 K (Fig. 10a, LCO-1373 thermal conductivity data are taken from [55] and are given for comparison). Samples thermal conductivity significantly depends on synthesis conditions, including the method and synthesis temperature, crystallites initial size, and tablet pressure pressing leading to different densities. The thermal conductivity values reported in the literature for unsubstituted $LaCoO_3$ near 300 K range from 0.9 [81] to 3.2 W/(K m) [82] (1.1 W/(K m) [18], 1.8 W/(K m) [66], 1.94 W/(K m) [40], 2.3 W/(K m) [16]). In the present study, the thermal conductivity of LCO(m)-1023 in the temperature range under study does not exceed 0.4 W/(K m), which is the minimum value for the thermal conductivity of unsubstituted lanthanum cobaltite near 300 K and is associated with the high sample porosity, lower sintering capacity (sample friability), and, possibly, with crystal structure second modification high content. Large (units of micrometers) and small (tens of nanometers) ceramic grains are poorly interconnected (Fig. 6b), which makes it difficult to phonon and electric charge transport. Therefore, we observe a decrease in thermal conductivity (Fig. 10a) and an increase in resistivity (Fig. 7a).

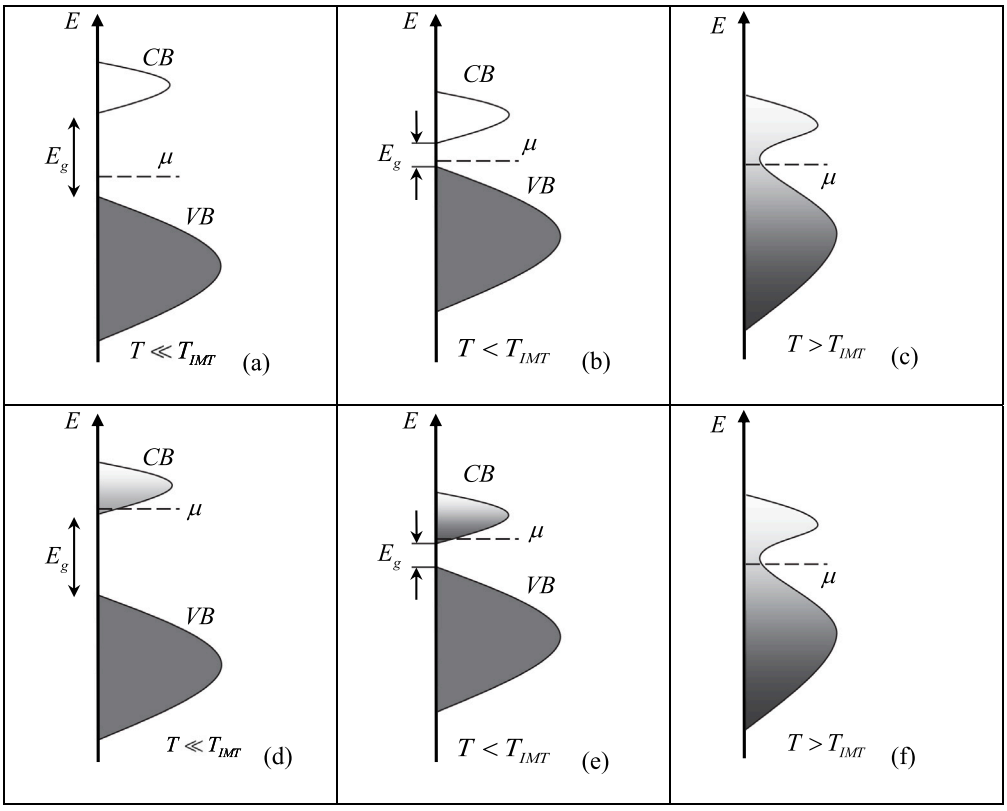

Fig. 9. LCO-1373 (a)–(c) and LCO(m)-1373 (d)–(f) samples electronic structure temperature dependence scheme.

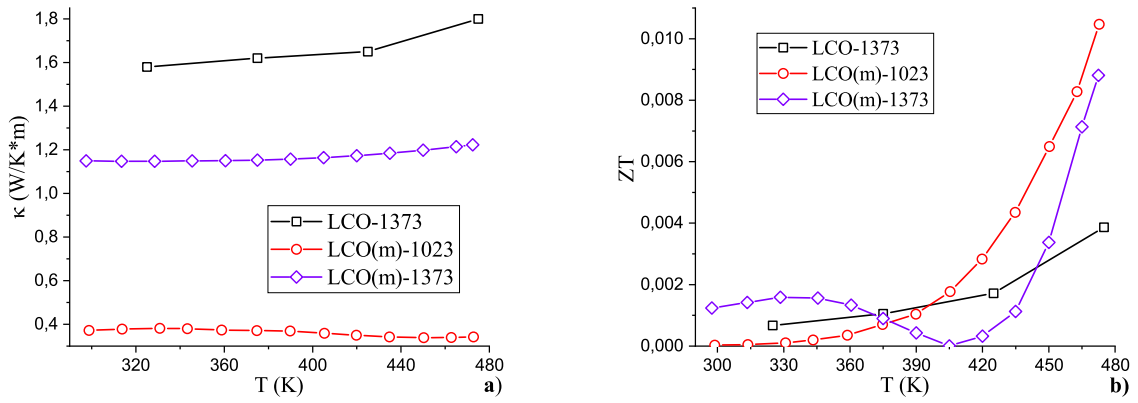

Fig. 10. Experimental thermal conductivity k (a) and dimensionless thermoelectric figure of merit ZT (b) temperature dependences.

3.3.4. Thermoelectric figure of merit

Calculated dimensionless thermoelectric figure of merit temperature dependences are shown in Fig. 10b. Due to the limited thermal conductivity measuring temperature range (300–480 K), it is not possible to estimate the synthesized samples quality factor maxima in the range up to 800 K. However, a more active ZT increase for LCO(m)-1023 and LCO(m)-1373 samples, synthesized from nanosized particles, in comparison with the LCO-1373 sample at temperatures above 400 K allows us to consider mechanical activation (high-energy grinding) as a way to increase the rare-earth cobalt oxides thermoelectric figure of merit.

4. Conclusions

Nanosized powders were obtained from the bulk formed LaCoO3 perovskite by high-energy grinding, from which $LaCoO_3$ samples were synthesized using standard ceramic technology at various temperatures and their crystal structure was studied. It was found that X-ray diffraction patterns are best described within the framework of a model that allows the coexistence of two domains in samples with the same crystal symmetry, but with different a and c lattice parameters. Domains ratio in the sample volume essentially depends on the initial particles size and the synthesis temperature. Maximum content of the second modification is observed in the sample synthesized from mechanically activated nanopowder at 1023 K and reaches 34%, for which the minimum thermal conductivity value of 0.4 W/(K m) is characteristic in the temperature range of 300–480 K. In the temperature range of 300–800 K, the electrical resistivity and the Seebeck coefficient were measured, and a comparative analysis of the thermoelectric properties was carried out depending on the sample preparation and annealing temperature. The maximum value of thermoelectric power factor of a

mechanically activated sample annealed at 1373 K is 2.5 times greater than that of a bulk sample. Mechanical activation and increase of synthesis temperature result in Seebeck coefficient sign change and a significant electrical resistivity decrease. ZT thermoelectric figure of merit sharp improvement for mechanically activated $LaCoO_3$ samples compared to a bulk sample at temperature above 400 K makes it possible to consider nanostructuring as a way to increase the rare-earth cobalt oxides thermoelectric figure of merit.

The observed two crystal structure modifications coexistence can be of significant importance in the formation of the $LaCoO_3$ magnetic properties and new thermoelectric materials creation based on rare-earth cobalt oxides with the properties of a phonon glass and an electronic crystal. Let us dwell on these two points in a little more detail. Our additional magnetic properties studies of the obtained samples have shown that among all of them, only the LCO(m)-1023 sample with the highest content of the second modification crystal structure exhibits ferromagnetism and magnetic hysteresis at $T = 2.2$ K. The ferromagnetic state in $LaCoO_3$ has long been discussed in the literature and manifests in epitaxial thin films, nanoparticles and precipitated powders, on the single crystals surface and ceramic grains (see, for example, [37,83–85]). In most works, it is associated with the surface effect and boundary interfaces (deformations, distortions, and defects in the crystal structure). According to our assumption, the second modification of the $LaCoO_3$ crystal structure is ferromagnetic, in contrast to the main nonmagnetic one at low temperatures, which causes the presence of a hysteresis loop for the LCO(m)-1023 sample. The presence of the two crystal structure modifications can be used to create new multiscale, spatially inhomogeneous thermoelectric materials with low thermal conductivity due to the efficient thermal phonons scattering by inhomogeneities of various scales. The thermoelectric energy conversion is a way to introduce energy-efficient technologies and environment conservation. This stimulates the search for new materials, engineering and technological solutions [86–88]

CRediT authorship contribution statement

Vyacheslav A. Dudnikov: Investigation, Methodology, Validation, Visualization, Writing – original draft, Writing – review & editing. **Yuri S. Orlov:** Conceptualization, Data curation, Investigation, Methodology, Project administration, Validation, Visualization, Writing – original draft, Writing – review & editing. **Leonid A. Solovyov:** Investigation, Methodology, Visualization. **Sergey N. Vereshchagin:** Data curation, Formal analysis, Investigation, Validation, Visualization, Writing – review & editing. **Yuri N. Ustyuzhanin:** Writing – review & editing. **Sergey M. Zharkov:** Data curation, Investigation, Visualization, Writing – review & editing. **Galina M. Zeer:** Investigation, Visualization. **Andrey A. Borus:** Resources. **Vitaly S. Bondarev:** Investigation, Visualization. **Sergey G. Ovchinnikov:** Formal analysis.

Declaration of competing interest

The authors declare that they have no known competing financial interests or personal relationships that could have appeared to influence the work reported in this paper.

Acknowledgments

This study was supported by the Russian Science Foundation, project no. 24-22-00091. The electron microscopy studies were carried out in the Siberian Federal University Joint Scientific Center.

References

[1] Ivanova NB, Ovchinnikov SG, Korshunov MM, Eremin IM, Kazak NV. Specific features of spin, charge, and orbital ordering in cobaltites. Phys – Uspekhi 2009;52:789–810.
[2] Raveau B, Seikh MdM. Cobalt oxides. In: From crystal chemistry to physics. Germany: Weinheim, Wiley-VCH; 2012.
[3] Bhide VG, Rajoria DS. Mossbauer studies of the high-spin-low-spin equilibria and the localized-collective electron transition in LaCoO3. Phys Rev B 1972;6:1021–32.
[4] Yan JQ, Zhou JS, Goodenough JB. Bond-length fluctuations and the spin-state transition in $LCoO_3$ (L=La, Pr, and Nd). Phys Rev B 2004;69:134409.
[5] Yamaguchi S, Okimoto Y, Tokura Y. Bandwidth dependence of insulator–metal transitions in perovskite cobalt oxides. Phys Rev B 1996;54:R11022–5.
[6] Knizek K, Jirak Z, Hejtmanek J, Veverka M, Marysko M, Maris G, et al. Structural anomalies associated with the electronic and spin transitions in $LnCoO_3$. Eur Phys J B 2005;47:213–20.
[7] Radaelli PG, Cheong SW. Structural phenomena associated with the spin-state transition in $LaCoO_3$. Phys Rev B 2002;66:094408.
[8] Zhou S, He L, Zhao S, Guo Y, Zhao J, Shi L. Size-dependent structural and magnetic properties of $LaCoO_3$ nanoparticles. J Phys Chem C 2009;113:13522–6.
[9] Ikeda A, Matsuda YH, Sato K, Ishii Yu, Sawabe H, Nakamura D, et al. Signature of spin–triplet exciton condensations in $LaCoO_3$ at ultrahigh magnetic fields up to 600 T. Nature Commun 2023;14:1744.
[10] Shu G-J, Wub PC, Chou FC. The spin–orbit-phonon coupling and crystalline elasticity of $LaCoO_3$ perovskite. RSC Adv 2020;10:43117–28.
[11] Scherrer B, Harvey AS, Tanasescu S, Teodorescu F, Botea A, Conder K, et al. Correlation between electrical properties and thermodynamic stability of $ACoO_{3-\delta}$ perovskites (A=La, Pr, Nd, Sm, Gd). Phys Rev B 2011;84:085113.
[12] Sahu Sulata Kumari, Tanasescu Speranta, Scherrer Barbara, Marinescu Cornelia, Navrotsky Alexandra. Energetics of lanthanide cobalt perovskites: $LnCoO_{3-\delta}$ (Ln=la, Nd, Sm, Gd). J Mater Chem A 2015;3:19490–6.
[13] Panfilov AS, Grechnev GE, Lyogenkaya AA, Pashchenko VA, Zhuravleva IP, Vasylechko LO, et al. Magnetic properties of $RCoO_3$ cobaltites (R=La, Pr, Nd, Sm, Eu). effects of hydrostatic and chemical pressure. Phys B: Condensed Matter 2019;553:80–7.
[14] Olsson Emilia, Aparicio-Angles Xavier, de Leeuw Nora H. Ab initio study of vacancy formation in cubic $LaMnO_3$ and $SmCoO_3$ as cathode materials in solid oxide fuel cells. J Chem Phys 2016;145:014703.
[15] Heikes RR, Miller RC, Mazelsky R. Magnetic and electrical anomalies in $LaCoO_3$. Physica 1964;30:1600–8.
[16] Berggold K, Kriener M, Zobel C, Reichl A, Reuther M, Muller R, et al. Thermal conductivity, thermopower, and figure of merit of $La_{1-x}Sr_xCoO_3$. Phys Rev B 2005;72:155116.
[17] Robert R, Aguirre MH, Hug P, Reller A, Weidenkaff A. High-temperature thermoelectric properties of $Ln(Co, Ni)O_3$ (Ln=la, Pr, Nd, Sm, Gd and Dy) compounds. Acta Mater 2007;55:4965–72.
[18] Kumar A, Sivaprahsam D, Thakur AD. Improvement of thermoelectric properties of lanthanum cobaltate by Sr and Mn co-substitution. J Alloys Compd 2018;735:1787–91.
[19] Androulakis J, Migiakis P, Giapintzakis J. $La_{0.95}Sr_{0.05}CoO_3$: An efficient room temperature thermoelectric oxide. Appl Phys Lett 2004;84:1099–101.
[20] Kumar A, Tomy CV, Thakur AD. Magnetothermopower, magnetoresistance and magnetothermal conductivity in $la_{0.95}sr_{0.05}co_{1-x}mn_xo_3$ $(0.00 \le x \le 1.00)$. Mater Res Express 2018;5:086110.
[21] Pei J, Chen G, Lu DQ, Liu PS, Zhou N. Synthesis and high temperature thermoelectric properties of $Ca_{3.0-x-y}Nd_xNa_yCo_4O_{9+\delta}$. Solid State Commun 2008;146:283–6.
[22] Kenfaui D, Chateigner D, Gomina M, Noudem JG. Texture, mechanical and thermoelectric properties of $Ca_3Co_4O_9$ ceramics. J Alloys Compd 2010;490:472–9.
[23] Koshibae W, Tsutsui K, Maekawa S. Thermopower in cobalt oxides. Phys Rev B 2000;62:6869–72.
[24] Terasaki I, Sasago Y, Uchinokura K. Large thermoelectric power in $NaCo_2O_4$ single crystals. Phys Rev B 1997;56:R12685.
[25] Mydeen K, Mandal P, Prabhakaran D, Jin CQ. Pressure- and temperature induced spin-state transition in single-crystalline $La_{1-x}Sr_xCoO_3$ $(x = 0.10$ and $0.33)$. Phys Rev B 2009;80:1–6.
[26] Kumar A. Dragoe D, Berardan D, Dragoe N. Thermoelectric properties of high-entropy rare-earth cobaltates. J Materiomics 2023;9:191–6.
[27] Shi Z, Gao F. Xu J, Zhu J, Zhang Y, Gao T, Qin M, et al. Two-step processing of thermoelectric $(Ca_{0.9}Ag_{0.1})_3Co_4O_9$/nano-sized ag composites with high ZT. J Eur Ceram Soc 2019;39:3088–93.
[28] Kumar A, Kumari K, Ray SJ, Thakur AD. Graphene mediated resistive switching and thermoelectric behavior in lanthanum cobaltate. J Appl Phys 2020;127:235103.
[29] Kumar A, Kumari K, Jayachandran B, Sivaprahsam D, Thakur AD. Thermoelectric properties of $(1-x)LaCoO_3/(x)La_{0.7}Sr_{0.3}MnO_3$ composite. J Alloys Compd 2018;749:1092–7.
[30] Kumar A, Kumari K, Jayachandran B, Sivaprahsam D, Thakur AD. Thermoelectric properties of $(1-x)LaCoO_3/(x)La_{0.95}Sr_{0.05}CoO_3$ composite. Mater Res Express 2019;6:055502.
[31] Kumar A, Dragoe D, Berardan D, Dragoe N. Improved thermoelectric properties in $(1-x)LaCoO_3/(x)La_{0.7}Sr_{0.3}CoO_3$ composite. Mater Chem Phys 2021;269:124750.

[32] Kumar A, Wojciechowski KT. Effect of interface thermal resistance on thermoelectric properties of acoustically mismatched composite. J Eur Ceram Soc 2022;42:4227–32.

[33] Fuchs D, Pinta C, Schwarz T, Schweiss P, Nagel P, Schuppler S, et al. Ferromagnetic order in epitaxially strained $LaCoO_3$ thin films. Phys Rev B 2007;75:144402.

[34] Yan JQ, Zhou JS, Goodenough JB. Ferromagnetism in $LaCoO_3$. Phys Rev B 2004;70:014402.

[35] Zhou S, Shi L, Zhao J, He L, Yang H, Zhang S. Ferromagnetism in $LaCoO_3$ nanoparticles. Phys Rev B 2007;76:172407.

[36] Wang Y, Fan HJ. Orbital ordering-driven ferromagnetism in $LaCoO_3$ nanowires. J Appl Phys 2010;108:053917.

[37] Harada A, Taniyama T, Takeuchi Y, Sato T, Kyomen T, Itoh M. Ferromagnetism at the surface of a $LaCoO_3$ single crystal observed using scanning SQUID microscopy. Phys Rev B 2007;75:184426.

[38] Yang Z, Huang Y, Dong B, Li HL, Shi SQ. Sol–gel template synthesis and characterization of $LaCoO_3$ nanowires. Appl Phys A 2006;84:117–22.

[39] Sathyamoorthy B, Gazzali PM, Murugesan C, Chandrasekaran G. Electrical properties of samarium cobaltite nanoparticles synthesized using Sol-Gel autocombustion route. Mater Res Bull 2014;53:169–76.

[40] Muraleedharan S, Davis N, Althaf R, Singh A, Ashok AM. Exploring the thermoelectric behavior of intrinsic and defect induced $LaCoO_3$ with selected alkaline earth metals. J Alloys Compd 2021;857:157507.

[41] Androulakis J, Katsarakis N, Giapintzakis J. Ferromagnetic and antiferromagnetic interactions in lanthanum cobalt oxide at low temperatures. Phys Rev B 2001;64:174401.

[42] Liang JJ, Weng HS. Catalytic properties of lanthanum strontium transition metal oxides ($La_{1-x}Sr_xBO_3$; B=manganese, iron, cobalt, nickel) for toluene oxidation. Ind Eng Chem Res 1993;32:2563–72.

[43] Spooren J, Walton RI, Millange F. A study of the manganites $La_{0.5}M_{0.5}MnO_3$ (M=Ca, Sr, Ba) prepared by hydrothermal synthesis. J Mater Chem 2005;15:1542–51.

[44] Zhang N, Liu E, Chen H, Hou J, Li C, Wan H. High-performance of $LaCoO_3/Co_3O_4$ nanocrystal as anode for lithium-ion batteries. Colloids Surf A 2021;628:127265.

[45] Matsumoto Y, Sasaki T, Hombo J. A new preparation method of lanthanum cobalt oxide, LaCoO3, perovskite using electrochemical oxidation. Inorganic Chem 1992;31:738–41.

[46] Cristobal AA, Botta PM, Aglietti EF, Conconi MS, Bercoff PG, Lopez JP. Synthesis, structure and magnetic properties of distorted $Y_xLa_{1-x}FeO_3$: Effects of mechanochemical activation and composition. Mater Chem Phys 2011;130:1275–9.

[47] Sompech S, Srion A, Nuntiya A. Synthesis of perovskite-type lanthanum cobalt oxide powders by mechanochemical activation method. ScienceAsia 2012;38:102–7.

[48] Solovyov LA. Full-profile refinement by derivative difference minimization. J Appl Crystallogr 2004;37:743–9.

[49] Burkov AT, Fedotov AI, Kasyanov AA, Panteleev RI, Nakama T. Methods and technique of thermopower and electrical conductivity measurements of thermoelectric materials at high temperatures. Sci Tech J Inform Technol Mech Opt 2015;15:173–95.

[50] Maris G, Ren Y, Volotchaev V, Zobel C, Lorenz T, Palstra TTM. Evidence for orbital ordering in $LaCoO_3$. Phys Rev B 2003;67:224423.

[51] Singh D, Choudhary N, Mahajan A, Singh S, Sharma S. Nanosized rare earth cobaltite $LaCoO_3$ synthesized by urea combustion method. Ionics 2015;21:1031–7.

[52] Berggold K, Kriener M, Becker P, Benomar M, Reuther M, Zobel C, et al. Anomalous expansion and phonon damping due to the Co spin-state transition in $RCoO_3$ (R=La, Pr, Nd, and Eu). Phys Rev B 2008;78:134402.

[53] Baier J, Jodlauk S, Kriener M, Reichl A, Zobel C, Kierspel H, et al. Spin-state transition and metal–insulator transition in $La_{1-x}Eu_xCoO_3$. Phys Rev B 2005;71:014443.

[54] Kharton VV, Figueiredo FM, Kovalevsky AV, Viskup AP, Naumovich EN, Yaremchenko AA, et al. Processing, microstructure and properties of $LaCoO_{3-\delta}$ ceramics. J Eur Ceram Soc 2001;21:2301–9.

[55] Li F, Li JF. Effect of Ni substitution on electrical and thermoelectric properties of $LaCoO_3$ ceramics. Ceram Int 2011;37:105–10.

[56] Robert R, Bocher L, Trottmann M, Reller A, Weidenkaff A. Synthesis and high-temperature thermoelectric properties of Ni and Ti substituted $LaCoO_3$. J Solid State Chem 2006;179:3893–9.

[57] Okazaki R, Tomiyasu K. Prominent electron–hole asymmetry in thermoelectric transport of $LaCoO_3$. Phys Rev B 2022;105:035154.

[58] Orlov YuS, Solovyov LA, Dudnikov VA, Fedorov AS, Kuzubov AA, Kazak NV, et al. Structural properties and high-temperature spin and electronic transitions in $GdCoO_3$: Experiment and theory. Phys Rev B 2013;88(1-14):235105.

[59] Hebert S, Flahaut D, Martin C, Lemonnier S, Noudem J, Goupil C, et al. Thermoelectric properties of perovskites: Sign change of the seebeck coefficient and high temperature properties. Progr Solid State Chem 2007;35:457–67.

[60] Jirak Z, Hejtmanek J, Knizek K, Veverka M. Electrical resistivity and thermopower measurements of the hole-and electron-doped cobaltites $LnCoO_3$. Phys Rev B 2008;78:014432.

[61] Sehlin SR, Anderson HU, Sparlin DM. Semiempirical model for the electrical properties of $La_{1-x}Ca_xCoO_3$. Phys Rev B 1995;52:11681.

[62] Dudnikov VA, Orlov YuS, Kazak NV, Fedorov AS, Solov'yov LA, Vereshchagin SN, et al. Effect of A-site cation ordering on the thermoelectric properties of the complex cobalt oxides $Gd_{1-x}Sr_xCoO_{3-\delta}$ ($x = 0.8$ and 0.9). Ceram Int 2018;44:10299–305.

[63] Taskin AA, Lavrov AN, Ando Y. Origin of the large thermoelectric power in oxygen-variable $RBaCo_2O_{5+x}$ (R=Gd, Nd). Phys Rev B 2006;73:121101.

[64] Dudnikov VA, Fedorov AS, Orlov YuS, Solovyov LA, Vereshchagin SN, Gavrilkin SYu, et al. Novikov SV and ovchinnikov SG, thermoelectric properties of the $SmCoO_3$ and $NdCoO_3$ cobalt oxides. Ceram Int 2020;46:17987–91.

[65] Fu L, Li JF. Preparation and thermoelectric properties of $LaCoO_3$ ceramics. Key Eng Mater 2010;434:404–8.

[66] Iwasaki K, Ito T, Nagasaki T, Arita Y, Yoshino M, Matsui T. Thermoelectric properties of polycrystalline $La_{1-x}Sr_xCoO_3$. J Solid State Chem 2008;181:3145–50.

[67] Asai K, Yoneda A, Yokokura O, Tranquada J, Shirane G, Kohn K. Two spin-state transitions in $LaCoO_3$. J Phys Soc Japan 1998;67:290–6.

[68] Saitoh T, Mizokawa T, Fujimori A, Abbate M, Takeda Y, Takano M. Electronic structure and temperature-induced paramagnetism in $LaCoO_3$. Phys Rev B 1997;55:4257–66.

[69] Klie RF, Zheng JC, Zhu Y, Varela M, Wu J, Leighton C. Direct measurement of the lowtemperature spin-state transition in $LaCoO_3$. Phys Rev Lett 2007;99:047203.

[70] Zobel C. Kriener M, Bruns D, Baier J, Gruninger M, Lorenz T, Reutler P, et al. Erratum: Evidence for a low-spin to intermediate-spin state transition in $LaCoO_3$ [physical review b 66 (2002) 020402(r)]. Phys Rev B 2005;71:019902.

[71] Hoch MJR, Nellutla S, Tol J, Choi ES, Lu J, Zheng H, et al. Diamagnetic to paramagnetic transition in $LaCoO_3$. Phys Rev B 2009;79:214421.

[72] Noguchi S, Kawamata S, Okuda K, Nojiri H, Motokawa M. Evidence for the excited triplet of Co^{3+} in $LaCoO_3$. Phys Rev B 2002;66:094404.

[73] Haverkort MW, Hu Z, Cezar JC, Burnus T, Hartmann H, Reuther M, et al. Spin state transition in $LaCoO_3$ studied using soft X-ray absorption spectroscopy and magnetic circular dichroism. Phys Rev Lett 2006;97:176405.

[74] Podlesnyak A, Streule S, Mesot J, Medarde M, Pomjakushina E, Conder K, et al. Spin-state transition in $LaCoO_3$: Direct neutron spectroscopic evidence of excited magnetic states. Phys Rev Lett 2006;97:247208.

[75] Podlesnyak A, Conder K, Pomjakushina E, Mirmelstein A, Allenspach P, Khomskii D. Effect of light Sr doping on the spin-state transition in $LaCoO_3$. J Magn Magn Mater 2007;310:1552–4.

[76] Rotter M, Wang ZS, Boothroyd AT, Prabhakaran D, Tanaka A, Doerr M. Mechanism of spin crossover in $LaCoO_3$ resolved by shape magnetostriction in pulsed magnetic fields. Sci Rep 2014;4:7003.

[77] Yamaguchi S, Okimoto Y, Taniguchi H, Tokura Y. Spin-state transition and high-spin polarons in $LaCoO_3$. Phys Rev B 1996;53. R2926(R).

[78] Ovchinnikov SG, Orlov YuS, Nekrasov IA, Pchelkina ZV. Electronic structure, magnetic properties, and mechanism of the insulator–metal transition in $LaCoO_3$ taking into account strong electron correlations. J Exp Theor Phys 2011;112:140–51.

[79] Zaanen J, Sawatzky GA, Allen JW. Band gaps and electronic structure of transition-metal compounds. Phys Rev Lett 1985;55:418.

[80] Liu Ran, Ge Yufei, Wang Dong, Shuai Zhigang. Understanding the temperature dependence of the seebeck coefficient from first-principles band structure calculations for organic thermoelectric materials. CCS Chem 2021;3:1477–83.

[81] Bousnina MA, Giovannelli F, Perriere L, Guegan G, Delorme F. Ba substitution for enhancement of the thermoelectric properties of $LaCoO_3$ ceramics ($0 \le x \le 0.75$). J Adv Ceram 2019;8:519–26.

[82] Pillai CGS, George AM. Thermal conductivity of $LaCoO_3$. Int J Thermophys 1983;4:183–8.

[83] Liu H, Shi L, Guo Y, Zhou S, Zhao J, Wang C, et al. Nature of ferromagnetic ordered state in $LaCoO_3$ epitaxial nano-thin film on $LaAlO_3$ substrate. J Alloys Compd 2014;594:158–64.

[84] Wu L, Chen M, Li C, Zhou J, Shen L, Wang Y, et al. Ferromagnetism and matrixdependent charge transfer in strained $LaMnO_3$-$LaCoO_3$ superlattices. Mater Res Lett 2018;6:501–7.

[85] Feng Qiyuan, Meng Dechao, Zhou Haibiao, Liang Genhao, Cui Zhangzhang, Huang Haoliang, et al. Direct imaging revealing halved ferromagnetism in tensile-strained $LaCoO_3$ thin films. Phys Rev Mater 2019;3:074406.

[86] Selimefendigil F, Oztop HF, Doranehgard MH. Impacts of elasticity and porosity of the channels on the performance features of thermoelectric module mounted system and efficient computations with multi-proper orthogonal decomposition approach. J Taiwan Inst Chem Eng 2021;124:359–68.

[87] Saeed Chani Muhammad Tariq, Bahadar Khan Sher, AM Asiri, Karimov KhS, Rub MA. Photothermoelectric cells based on pristine α-Al_2O_3 co-doped CdO, CNTs and their single and bi-layer composites with silicone adhesive. J Taiwan Inst Chem Eng 2015;52:93–9.

[88] Wang SL, Liu HB, Gao YW, Shen Yu, Yang YR, Wang XD, et al. Transient supercooling performance of thermoelectric coolers with a continuous double current pulse. J Taiwan Inst Chem Eng 2021;120:127–35.